ChemComm

COMMUNICATION

View Article Online
View Journal | View Issue

Cite this: *Chem. Commun.*, 2023, 59, 12031

Received 29th June 2023,
Accepted 11th September 2023

DOI: 10.1039/d3cc03131d

rsc.li/chemcomm

Selective adsorption of polycyclic aromatic hydrocarbons by isostructural hydrogen-bonded organic frameworks†

Peng Cui, *[abc] Qiang Zhu,[b] Fangfang Zhang,[a] Dongni Liu[ad] and Wenshuai Zhu*[ac]

Two isostructural hydrogen-bonded organic frameworks (HOFs) with 1-D hexagonal-shaped pores were crystallised using the molecules biphenyl-3,3′,5,5′-tetracarboxylic acid (BPTCA) and [1,1′:4′,1″]terphenyl-3,3″,5,5″-tetracarboxylic acid (TPTCA). The desolvated HOFs, named BPTCA-2 and TPTCA-2, exhibited selective adsorption towards naphthalene and anthracene, respectively, during competitive adsorption experiments.

Polycyclic aromatic hydrocarbons (PAHs) are organic environmental pollutants and by-products from the catalytic cracking of diesel.[1] PAHs also play an important role in the chemical industry, such as the preparation of dyes, pesticides and resins.[2] The removal of PAHs from diesel improves the purity and extracts industrially important feedstocks. Porous materials, such as metal organic frameworks (MOFs),[3] porous organic cages,[4] covalent organic frameworks (COFs),[5–7] porous aromatic frameworks (PAFs),[8] and hypercrosslinked polymers (HCPs)[9] have been explored as PAHs adsorbents. However, porous adsorbents with selective adsorption abilities for different PAHs are less common.

Hydrogen-bonded organic frameworks (HOFs) are an exciting class of crystalline material that has more recently been explored as porous solids.[10] HOFs are constructed from organic molecules and stabilised by non-covalent interaction, such as hydrogen bonding and π–π interactions.[11] Due to the inherent flexibility of hydrogen bonds and the solubility of the building blocks, HOFs offer some advantages, such as easy purification and regeneration, solution processability, and synthetic tuneability.[12] Early reports of HOFs include the interpenetrated form of trimesic acid (α-TMA).[13] Several groups have recently explored the crystallisation of non- or low-interpenetrated porous HOFs, which have been used for gas storage,[14] molecular separation,[15] and enzyme encapsulation.[16] Also, computational methods, such as crystal structure prediction (CSP) and high throughput (HT) crystallisation, have been used to accelerate the discovery of porous HOFs.[17] However, a combination of weaker and flexible non-covalent interactions in HOFs can lead to poor structural stability, particularly for HOFs with low skeleton densities. This instability can lead to the collapse and rearrangement of HOFs during desolvation of the crystal pores.[18]

HOFs with permanent porosities have been reported to adsorb various organic molecules.[19] They exhibit pores ranging from micropores (*e.g.*, 3.4 × 5.3 Å)[20] to mesopores (*e.g.*, 2.8 nm),[21] which has been achieved by adjusting the symmetry, size, and functionality of the building blocks.[21,22] For example, two isostructural HOFs, T2-γ and T2E-α with 2 nm and 2.8 nm pores, respectively, were assembled using triptycene-based building blocks with benzimidazolone groups.[21] Pyrene-based building blocks have been used to prepare isostructural HOFs, including HOF-102, which has been used for storing biomolecules and photochemically detoxifying mustard gas.[23–25]

In this study, we used two building blocks containing biphenyl (**BPTCA**) and terphenyl (**TPTCA**) cores, each functionalised with four carboxylic acid groups, to construct isostructural HOFs with 1-D hexagonal-shaped pores (Fig. 1a). **BPTCA** and **TPTCA** are structurally related to 1,2,4,5-benzenetetracarboxylic acid (**BTCA**, Fig. 1b), which was reported to form a water solvate in 1971.[26] Subsequently, **BTCA** was reported to form a square grid network that features R_2^2 (8) hydrogen bonding interactions by Biradha Group,[27] using phenol solvent that occupied the pores (Fig. 1b). Here, we focussed on the larger isostructural analogues **BPTCA** and **TPTCA** (Fig. 1b). **BPTCA** was reported to assemble into 3-fold interpenetrated

[a] *School of Chemistry and Chemical Engineering, Jiangsu University, Zhenjiang, 212013, PR China*
[b] *Department of Chemistry and Materials Innovation Factory, University of Liverpool, Liverpool, L7 3NY, UK*
[c] *College of Chemical Engineering and Environment, State Key Laboratory of Heavy Oil Processing, China University of Petroleum-Beijing, Beijing, 102249, PR China. E-mail: P.Cui@ujs.edu.cn, zhuws@cup.edu.cn*
[d] *School of Materials Science and Engineering, Jiangsu University, Zhenjiang, 212013, PR China*

† Electronic supplementary information (ESI) available. CCDC 2277044 and 2277046–2277049. For ESI and crystallographic data in CIF or other electronic format see DOI: https://doi.org/10.1039/d3cc03131d

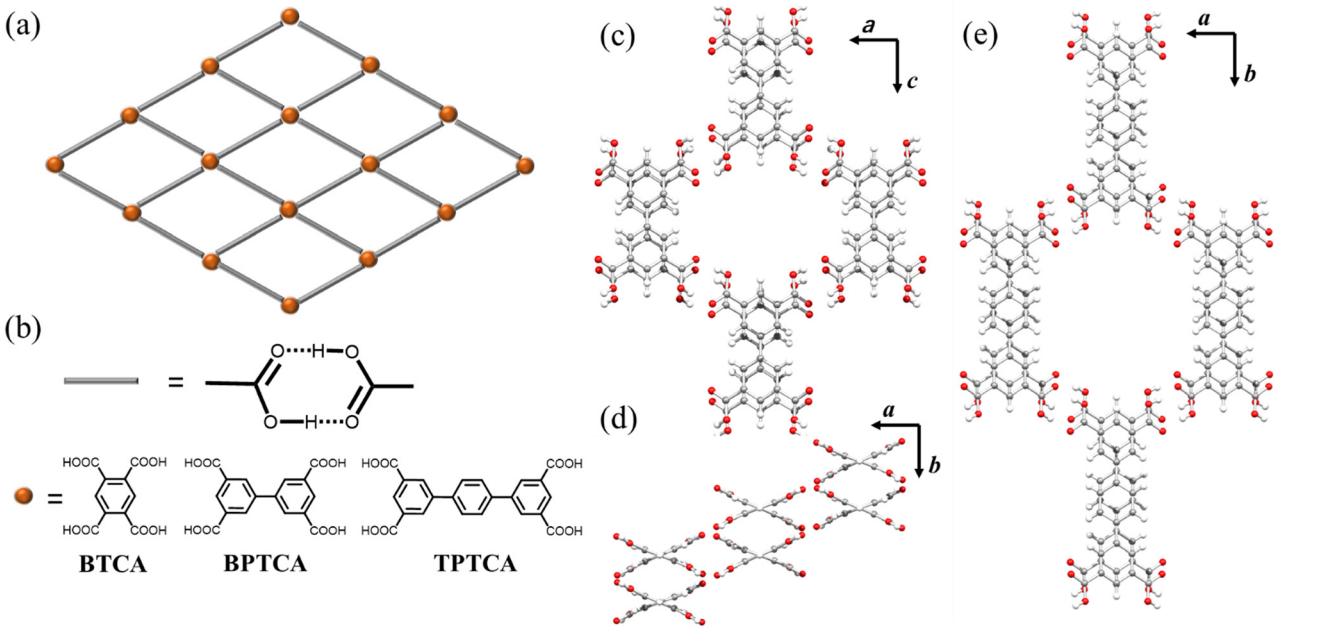

Fig. 1 (a) The diagram of the **sql** net often found in layered HOFs; (b) The R_2^2 (8) hydrogen bonding interactions and the molecular structures of **BTCA**, **BPTCA**, and **TPTCA**; (c) The A-B-type packing mode in **BPTCA-1** viewed along the *b*-axis; (d) **BPTCA-1** viewed along the *c*-axis; (e) The A-B-type packing mode of **TPTCA-1** viewed along the *c*-axis. Solvent molecules in the crystal pores are omitted for clarity. Grey: carbon, red: oxygen, white: hydrogen.

HOF under hydrothermal conditions on cooling from 503 K.[28] The surface assembly of **BPTCA** and **TPTCA** on Au(111)[29] and nonanoic acid/graphite interfaces[30] have also been explored. However, to our knowledge, the formation of non-interpenetrated porous HOF using **BPTCA** and **TPTCA** has not been reported.

Here, we attempted to crystallise **BPTCA** and **TPTCA** from a range of crystallisation solvents and obtained colourless needle shape crystals of **BPTCA-1** and **TPTCA-1** from DMF and $CHCl_3$ solvent mixtures (see ESI,† Sections 2.1 and 2.3). The solvated single crystal X-ray diffraction (SC-XRD) structures showed that the phenyl groups of **BPTCA** in **BPTCA-1** and **TPTCA** in **TPTCA-1** adopt twisted conformations (Fig. 1). In **BPTCA-1**, the phenyl groups in **BPTCA** are twisted by 42.6° (Fig. 1d). In the **BPTCA-1** structure, the **BPTCA** molecules hydrogen-bond to four other **BPTCA** molecules through R_2^2 (8) interactions to generate distorted hexagonal-shaped pores (Fig. 1c). These pores pass through the offset, A-*B*-type, π–π stacked layers of **BPTCA** molecules, which are separated by ~3.7 Å and an offset of ~1.4 Å (Fig. 1c). The SC-XRD structure of **TPTCA-1** showed that **TPTCA** adopts a non-planar conformation with the phenyl group twisted by 31.4° and 35.9°. In the extended **TPTCA-1** structure, **TPTCA**, like **BPTCA** in **BPTCA-1**, hydrogen-bonds to four neighbouring **TPTCA** through R_2^2 (8) hydrogen bonding interactions to assemble into a HOF with hexagonal-shaped pores (Fig. 1e). The **TPTCA** molecules also stack in offset, π–π stacked ''A-B'' layers in **TPTCA-1** (Fig. 1e), which are separated by ~3.7 Å and offset is ~1.2 Å. Disordered solvent occupies the 1-D channels in **BPTCA-1** and **TPTCA-1**, which we could not model accurately in the SC-XRD structures (Fig. S1 and S3, ESI†).

To evacuate the solvent-filled pores of **BPTCA-1** and **TPTCA-1**, we first exchanged the crystallisation solvents by immersing the **BPTCA-1** and **TPTCA-1** crystals in *n*-pentane for five days. Then, we degassed the samples under a dynamic vacuum at room temperature for 2 hours to obtain **BPTCA-2** and **TPTCA-2**. The SC-XRD structure showed that both **BPTCA-2** and **TPTCA-2** had non-interpenetrated porous frameworks after activation under these conditions. However, in **BPTCA-2**, the **BPTCA** molecules transformed into an A-B-C-type stacked structure, which we attribute to the slippage of the layers of **BPTCA** molecules along the *c*-axis (Fig. S2, ESI†). This structural transformation reduced the dihedral angle between the two-phenyl rings from 42.6° in **BPTCA-1** to 35.1° in **BPTCA-2**. Despite the transformation, **BPTCA-2** retained its 1-D pores, which we calculated had the dimensions 11.3 Å × 8.6 Å. The SC-XRD structure of **TPTCA-2** (Fig. S4, ESI†) is comparable to **TPTCA-1**, and we calculated that the dimensions of the 1-D pores were 12.4 Å × 11.3 Å (Fig. 1e).

We recorded N_2 sorption isotherms at 77 K to measure the surface areas of **BPTCA-2** and **TPTCA-2**. Before the N_2 sorption isotherms, we degassed the samples for 12 hours at RT. After activation under these conditions, the Brunauer–Emmett–Teller surface areas (SA_{BET}) of **BPTCA-2** (15 $m^2\ g^{-1}$, Fig. S5, ESI†) and **TPTCA-2** (30 $m^2\ g^{-1}$, Fig. S6, ESI†) were low. We attribute the low SA_{BET} of **BPTCA-2** to a decrease in the crystallinity of the sample and a change in the structure observed by PXRD after degassing (Fig. S7, ESI†). We could not determine the SC-XRD of **BPTCA** after the sorption measurement. However, after the sorption measurement, we determined a new SC-XRD structure of **TPTCA-2**, named **TPTCA-2_degas**. The SC-XRD structure of **TPTCA-2_degas** showed a slippage of the 2-D

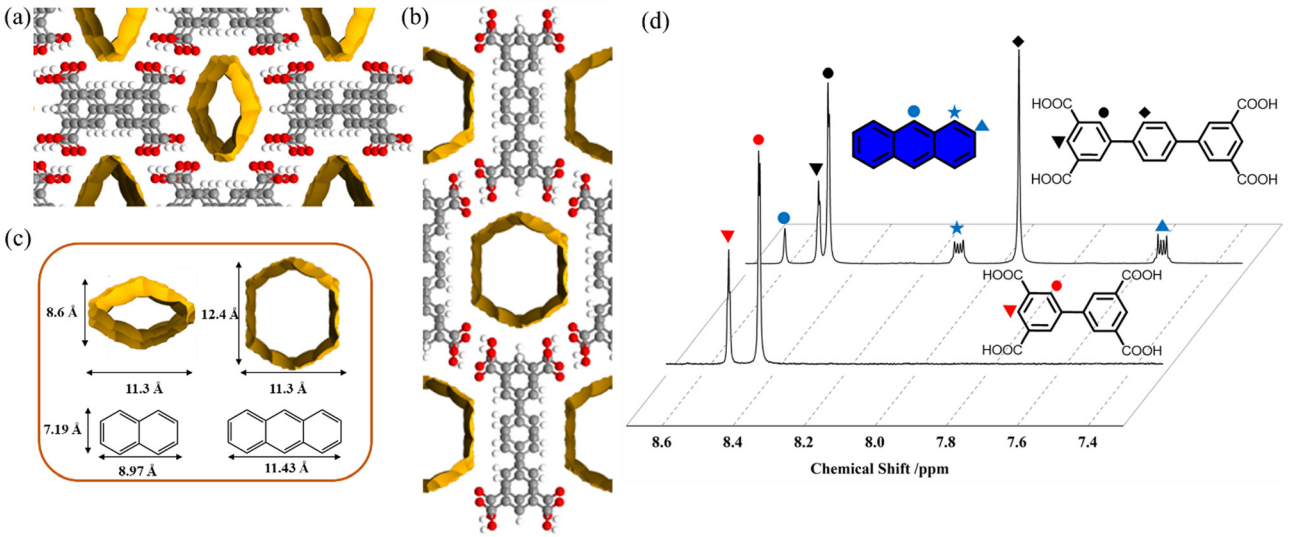

Fig. 2 (a) Crystal packing diagram of **BPTCA-2** and (b) **TPTCA-2** viewed along the crystallographic *a*-axis with the walls of the 1-D pores highlighted in yellow; (c) The size of the solvent-accessible voids in **BPTCA-2** and **TPTCA-2** compared to the dimensions of the **NA** and **AN** molecules, the solvent-accessible space (1.4 Å probe radius, 0.1 Å grid spacing was used in Mercury) is shown with yellow; (d) The ^{1}H NMR spectrum of **BPTCA-2**⊃**AN** and **TPTCA-2**⊃**AN**. The characteristic peaks of **BPTCA**, **TPTCA**, and **AN** molecules are marked with red, black, and blue symbols, respectively.

sql nets, hydrogen-bonded **TPTCA** layers, in comparison to **TPTCA-2**, which led to the dimension of the pores shrinking to 5.9 Å × 3.4 Å (Fig. S8, ESI†). This **sql** nets, hydrogen-bonded **TPTCA** layers also changed from being planar in **TPTCA-2** to a wave-like structure in **TPTCA-2_degas** (Fig. S9, ESI†). The structural transformation that we observed during degassing proved that **TPTCA-2** is metastable, which agrees with the PXRD data (Fig. S10, ESI†). We likewise attribute the low SA_{BET} of **TPTCA-2** to a decrease in the crystallinity of the sample and a change in structure during degassing.

To further explore the porosity of **BPTCA-2** and **TPTCA-2**, we investigated the adsorption of different PAHs at room temperature. We selected naphthalene (**NA**, 9.0 Å × 7.2 Å, Fig. 2c) and anthracene (**AN**, 11.4 Å × 7.2 Å, Fig. 2c) as adsorbates because they have dimensions that are similar to the pore sizes in **BPTCA-2** (11.3 Å × 8.6 Å, Fig. 2a and c) and **TPTCA-2** (12.4 Å × 11.3 Å, Fig. 2b and c). We performed these measurements by immersing **BPTCA-2** and **TPTCA-2** solids (3 mg) in *n*-hexadecane solutions that contained **NA** or **AN** dissolved at concentrations of 200 ppm. Then, we collected the **BPTCA-2** and **TPTCA-2** solids by filtration and washed them with pure *n*-hexadecane before analysis. The crystallinity of **BPTCA-2** and **TPTCA-2** solids after immersion in the *n*-hexadecane solutions was insufficient for analysis with SC-XRD. Therefore, we used ^{1}H NMR spectra to determine the **NA** and **AN** host: guest ratios in the **BPTCA-2** and **TPTCA-2** solids after dissolving the HOFs in deuterated dimethyl sulfoxide (DMSO-d_6). We observed signals in the NMRs of the dissolved solids that indicated **NA** was adsorbed from the *n*-hexadecane solution by **BPTCA-2** and **TPTCA-2** (Fig. S11, ESI†). The host: guest ratio based on the NMR data was estimated to be 1 : 0.063 for **BPTCA-2**⊃**NA** (Fig. S11 and S12, ESI†) and 1 : 0.11 for **TPTCA-2**⊃**NA** (Fig. S11 and S12, ESI†). Fig. 2d shows the ^{1}H NMR spectra of the dissolved **BPTCA-2** and **TPTCA-2** solids after immersion in the **AN***n*-hexadecane solution. By comparison, we only observed **AN** signals in the ^{1}H NMR spectrum of the dissolved **TPTCA-2** solid, which indicates that **AN** was not adsorbed by the **BPTCA-2** solid. The host: guest ratios based on this NMR data were, therefore, estimated to be 1 : 0.2 for **TPTCA-2**⊃**AN**, and tentatively 1 : 0 for **BPTCA-2**⊃**AN** (Fig. 2d). Based on the relative integrals from the ^{1}H NMR spectra, the adsorption capacities of **BPTCA-2** for **NA** and **AN** are 24.3 mg g^{-1} and 0 mg g^{-1}, respectively, and of **TPTCA-2** for **NA** and **AN** are 35.0 mg g^{-1} and 87.8 mg g^{-1}, respectively.

We also used gas chromatography (GC) to investigate the adsorption properties of **BPTCA-2** and **TPTCA-2**. The GC data showed a similar trend in absorption capacities (28.5 mg g^{-1} for **BPTCA-2**⊃**NA**; 41.2 mg g^{-1} for **TPTCA-2**⊃**NA**; 93.8 mg g^{-1} for **TPTCA-2**⊃**AN**), which indicates that **BPTCA-2** and **TPTCA-2** are promising PAHs adsorbents.

To explore the selective adsorption ability of **TPTCA-2** towards **NA** and **AN**, we immersed **TPTCA-2** crystal in *n*-hexadecane containing 200 ppm **NA** and **AN**. From the competitive adsorption experiment, we observed that **TPTCA-2** exhibited the selective adsorption of **AN**, while no **NA** appeared to be adsorbed from the **NA** and **AN** mixture by the ^{1}H NMR spectrum (Fig. S13, ESI†). We attribute this observation to the stronger CH···π interactions between **AN** and **TPTCA-2**.

We also investigated the selective adsorption of **NA** and **AN** by **BPTCA-2** and **TPTCA-2** using UV-vis spectroscopy (Fig. 3 and Fig. S14, ESI†). The UV-vis spectra showed that the absorbance intensity of **NA** and **AN** decreased over time after the addition of the **BPTCA-2** and **TPTCA-2** solids. The adsorption of **AN** appeared to reach equilibrium after 3 hours, which indicated that the PAHs were adsorbed by the HOFs (Fig. 3 and Fig. S14, ESI†).

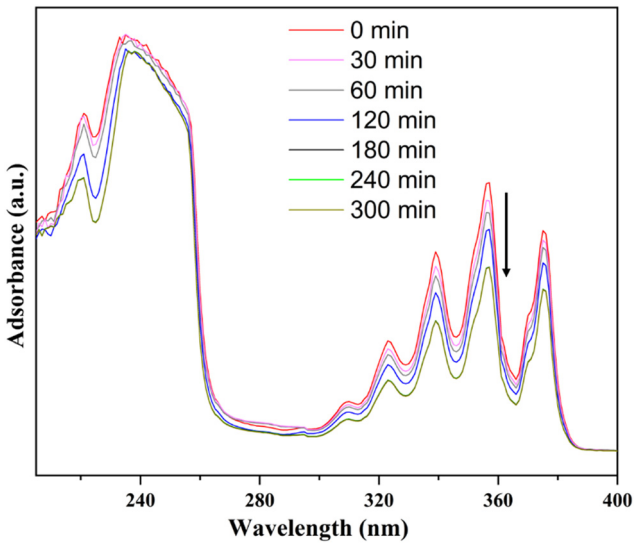

Fig. 3 The UV-vis spectra of *n*-hexadecane solution containing 200 ppm of **AN** after the addition of **TPTCA-2** solid.

In summary, we have found two isostructural HOFs with hexagonal-shaped pores, **BPTCA-1** and **TPTCA-1**, which crystallised from DMF and $CHCl_3$ solvent mixtures. After degassing the activated crystals, **BPTCA-2** and **TPTCA-2**, both HOFs had low SA_{BET} due to a combination of amorphous particles and structural transformations. However, the **BPTCA-2** and **TPTCA-2** showed good porosity for PAHs. Moreover, the **BPTCA-2** exhibited exclusive perfect selectivity towards **NA** over **AN**, while **TPTCA-2** showed selectivity towards **AN** from **NA**, which was determined by ^{1}H NMR and UV-vis spectroscopy. The selective adsorption results provided an effective adsorption method towards to PAHs with different sizes using HOF adsorbents, demonstrating the potential of **BPTCA-2** and **TPTCA-2** as industrially relevant adsorbents for **NA** and **AN** in the petrochemical industry.

For funding, the authors acknowledge the Engineering and Physical Sciences Research Council (EPSRC) (EP/N004884/1), the National Natural Science Foundation of China (22308124), the Jiangsu University Funding (5501310018), the Leverhulme Trust *via* the Leverhulme Research Centre for Functional Materials Design. The authors acknowledge Dr Marc Little and Prof. Andrew Cooper for single crystal structure refinement and manuscript revisions. The authors thank Diamond Light Source for access to beamlines I19 (CY21726).

Conflicts of interest

There are no conflicts to declare.

Notes and references

1 X. Qin, L. Ye, L. Hou, T. Wang, M. Ma, X. Pu, X. Han, J. Liu, B. Luan and P. Liu, *Chem. Eng. J.*, 2023, **466**, 143078.
2 D. S. N. Parker and R. I. Kaiser, *Chem. Soc. Rev.*, 2017, **46**, 452–463.
3 R. Sekiya and S. Nishikiori, *Chem. Commun.*, 2012, **48**, 5022.
4 C. F. Espinosa, T. K. Ronson and J. R. Nitschke, *J. Am. Chem. Soc.*, 2023, jacs.3c00661.
5 H. Zhou, C. Zhou, S. Tang, F. Zhang, S. Lei, Z. Li, J. Liu and M. Chen, *Mater. Lett.*, 2022, **307**, 131002.
6 S. Karak, K. Dey, A. Torris, A. Halder, S. Bera, F. Kanheerampockil and R. Banerjee, *J. Am. Chem. Soc.*, 2019, **141**, 7572–7581.
7 H. S. Sasmal, A. Kumar Mahato, P. Majumder and R. Banerjee, *J. Am. Chem. Soc.*, 2022, **144**, 11482–11498.
8 Y. Yuan and G. Zhu, *ACS Cent. Sci.*, 2019, **5**, 409–418.
9 J. Li, B. Zhao, L. Guo, Z. Wang, C. Wang, Z. Wang, S. Zhang and Q. Wu, *J. Chromatogr. A*, 2021, **1653**, 462428.
10 L. Chen, B. Zhang, L. Chen, H. Liu, Y. Hu and S. Qiao, *Mater. Adv.*, 2022, **3**, 3680–3708.
11 Z.-J. Lin, S. A. R. Mahammed, T.-F. Liu and R. Cao, *ACS Cent. Sci.*, 2022, **8**, 1589–1608.
12 P. Li, M. R. Ryder and J. F. Stoddart, *Acc. Mater. Res.*, 2020, **1**, 77–87.
13 D. J. Duchamp and R. E. Marsh, *Acta Crystallogr., Sect. B: Struct. Crystallogr. Cryst. Chem.*, 1969, **25**, 5–19.
14 B. Wang, X.-L. Lv, J. Lv, L. Ma, R.-B. Lin, H. Cui, J. Zhang, Z. Zhang, S. Xiang and B. Chen, *Chem. Commun.*, 2020, **56**, 66–69.
15 S. Feng, Y. Shang, Z. Wang, Z. Kang, R. Wang, J. Jiang, L. Fan, W. Fan, Z. Liu, G. Kong, Y. Feng, S. Hu, H. Guo and D. Sun, *Angew. Chem., Int. Ed.*, 2020, **59**, 3840–3845.
16 R.-B. Lin and B. Chen, *Nat. Chem.*, 2019, **11**, 1078–1080.
17 P. Cui, D. P. McMahon, P. R. Spackman, B. M. Alston, M. A. Little, G. M. Day and A. I. Cooper, *Chem. Sci.*, 2019, **10**, 9988–9997.
18 Y. Shi, S. Wang, W. Tao, J. Guo, S. Xie, Y. Ding, G. Xu, C. Chen, X. Sun, Z. Zhang, Z. He, P. Wei and B. Z. Tang, *Nat. Commun.*, 2022, **13**, 1882.
19 X. Song, Y. Wang, C. Wang, D. Wang, G. Zhuang, K. O. Kirlikovali, P. Li and O. K. Farha, *J. Am. Chem. Soc.*, 2022, **144**, 10663–10687.
20 Y. Chen, Y. Yang, Y. Wang, Q. Xiong, J. Yang, S. Xiang, L. Li, J. Li, Z. Zhang and B. Chen, *J. Am. Chem. Soc.*, 2022, **144**, 17033–17040.
21 A. Pulido, L. Chen, T. Kaczorowski, D. Holden, M. A. Little, S. Y. Chong, B. J. Slater, D. P. McMahon, B. Bonillo, C. J. Stackhouse, A. Stephenson, C. M. Kane, R. Clowes, T. Hasell, A. I. Cooper and G. M. Day, *Nature*, 2017, **543**, 657–664.
22 Y. Suzuki, M. Gutiérrez, S. Tanaka, E. Gomez, N. Tohnai, N. Yasuda, N. Matubayasi, A. Douhal and I. Hisaki, *Chem. Sci.*, 2021, **12**, 9607–9618.
23 K. Ma, P. Li, J. H. Xin, Y. Chen, Z. Chen, S. Goswami, X. Liu, S. Kato, H. Chen, X. Zhang, J. Bai, M. C. Wasson, R. R. Maldonado, R. Q. Snurr and O. K. Farha, *Cell Rep. Phys. Sci.*, 2020, **1**, 100024.
24 Y. Wang, K. Ma, J. Bai, T. Xu, W. Han, C. Wang, Z. Chen, K. O. Kirlikovali, P. Li, J. Xiao and O. K. Farha, *Angew. Chem., Int. Ed.*, 2022, **61**, e202115956.
25 C. Wang, Y. Wang, K. O. Kirlikovali, K. Ma, Y. Zhou, P. Li and O. K. Farha, *Adv. Mater.*, 2022, **34**, 2202287.
26 F. Takusagawa, K. Hirotsu and A. Shimada, *Bull. Chem. Soc. Jpn.*, 1971, **44**, 1274–1278.
27 L. Rajput, N. Jana and K. Biradha, *Cryst. Growth Des.*, 2010, **10**, 4565–4570.
28 S. J. Coles, R. Holmes, M. B. Hursthouse and D. J. Price, *Acta Crystallogr., Sect. E: Struct. Rep. Online*, 2002, **58**, o626–o628.
29 I. Cebula, E. F. Smith, M. D. C. Gimenez-Lopez, S. Yang, M. Schröder, N. R. Champness and P. H. Beton, *J. Phys. Chem. C*, 2013, **117**, 18381–18385.
30 R. Steeno, A. Minoia, M. C. Gimenez-Lopez, M. O. Blunt, N. R. Champness, R. Lazzaroni, K. S. Mali and S. De Feyter, *Chem. Commun.*, 2021, **57**, 1454–1457.

